EES Batteries

PAPER

View Article Online
View Journal | View Issue

Cite this: *EES Batteries*, 2025, **1**, 1301

Enhancing lithium-ion desolvation with robust polyhydroquinone-diimidazopyridine nanofibers for high-rate Li–S batteries

Hao Yang,†[a] Haoyu Liu, †[a] Jia Zhang,†[a] Tao Zhang, [a] Xiaoqing Zhu, [a] Zhongxiu Liu,[a] Liping Zhu, *[a] Changyong (Chase) Cao,[b] Guiyin Xu *[a] and Meifang Zhu [a]

Lithium–sulfur (Li–S) batteries have attracted considerable attention due to their high energy density. Nevertheless, the shuttle effect of lithium polysulfides (LiPSs) and the growth of lithium dendrites remain primary issues hindering their commercial application. Herein, a novel functional separator based on a polypropylene (PP) matrix is proposed, modified with an ultrathin poly[2,6-diimidazo(4,5-*b*:4′,5′-*e*)pyridinylene-1,4(2,5-dihydroxy)phenylene] (PIPD) nanofiber layer *via* a scalable blade-coating process. Compared to unmodified PP, the PIPD-coated separator demonstrates significantly enhanced mechanical strength. The PIPD nanofiber coating demonstrates superior lithiophilicity, effectively reducing the lithium-ion desolvation energy barrier while enhancing deposition kinetics, thereby promoting the formation of uniform lithium nucleation sites. Additionally, the imidazole groups in PIPD act as Lewis acids, notably adsorbing Lewis-based LiPSs and mitigating the shuttle effect. Consequently, Li||Li cells assembled with modified separators demonstrated stable cycling over 1800 hours at 1 mA cm^{-2}/1 mAh cm^{-2}. Remarkably, Li–S batteries demonstrated a specific capacity retention of 728.9 mAh g^{-1} after 450 cycles at 3C, with an ultralow capacity fade rate of only 0.072% per cycle. The proposed innovative strategy enhances the performance and safety of Li–S batteries, paving the way for their commercial viability in advanced energy storage applications.

Received 1st May 2025,
Accepted 28th July 2025

DOI: 10.1039/d5eb00085h

rsc.li/EESBatteries

Broader context

Lithium–sulfur (Li–S) batteries are considered one of the most promising next-generation battery technologies due to their high theoretical energy density. They have the advantages of low cost and high capacity, but the cathode shuttle effect and the growth of anode lithium dendrites have hindered their development. Among the various modification strategies, nanofiber composite separator modification offers a promising approach for addressing issues on both anodes and cathodes. Here, an innovative approach is developed by combining an ultrathin poly[2,6-diimidazo(4,5-*b*:4′,5′-*e*)pyridinylene-1,4(2,5-dihydroxy) phenylene] (PIPD) nanofiber coating (1 μm) with a polypropylene (PP) matrix to develop a functional separator (PP@PIPD). Benefiting from its high dipole moment (stronger molecular polarity compared to alkyl groups), PIPD enables excess electrons promoting the decomposition of LiTFSI and generation of LiF, thus forming a stable solid electrolyte interphase (SEI). In addition, precipitation kinetics of polysulfides were accelerated by promoting the desolvation of Li^+. This work elucidates the critical impact of Li^+ desolvation on high-rate Li–S batteries. The batteries with the PP@PIPD separator possessed superior competitiveness in terms of average capacity fading, initial capability, coulombic efficiency and long-term cyclability, compared with the Li–S batteries with the reported separators, demonstrating promising prospects for developing Li–S batteries.

Introduction

The expanding requirements for energy storage infrastructure, driven by the accelerating adoption of renewable energy generation and electric mobility, mandate technological breakthroughs in next-generation battery systems.[1,2] Li–S batteries have garnered extensive attention owing to their theoretical energy density of 2600 Wh kg^{-1}, outperforming that of conventional lithium-ion batteries.[3] However, the commercialization of Li–S batteries confronts severe hurdles, mainly affected by the shuttle effect of polysulfides and slow redox kinetics of sulfur, which collectively result in rapid capacity deterioration.[4] Moreover, the shuttling of LiPSs compromises the structural integrity of the solid electrolyte interphase (SEI), accelerating lithium dendrite growth and posing critical safety

[a]*State Key Laboratory of Advanced Fiber Materials, College of Materials Science and Engineering, Donghua University, Shanghai 201620, China.*
E-mail: zhulp@dhu.edu.cn, xuguiyin@dhu.edu.cn
[b]*Laboratory for Soft Machines & Electronics, Department of Mechanical and Aerospace Engineering, Case Western Reserve University, Cleveland, OH 44106, USA*
†These authors contribute equally to this paper.

concerns.[5] The key to addressing these challenges lies in optimizing the reaction kinetics of LiPSs and stabilizing the SEI, which are critical for the commercial application of Li–S batteries.

Various strategies have been proposed to mitigate these issues, focusing on sulfur host optimization using conductive carbon or porous materials to anchor LiPSs,[6,7] the introduction of catalysts aimed at improving sulfur reaction kinetics,[8] and the use of functional electrolytes to stabilize the SEI.[9] Despite these efforts, the practical application of Li–S batteries remains constrained by the slow conversion kinetics of LiPSs and instability of the SEI. The separator serves as an important component, whose performance directly affects the cycling stability of battery systems.[10] Conventional polyolefin-based separators (polypropylene (PP) and polyethylene (PE)) fail to suppress dendritic growth and polysulfide shuttle due to their large, uneven pores and non-polar nature.[11]

Recent research studies have highlighted the potential of modifying commercial separators with functional coatings to address these limitations. Various coatings, including organic polymers (*e.g.*, cellulose derivatives,[12,13] polybenzimidazoles,[14,15] polyimides[16,17]), inorganic materials (*e.g.*, transition metal phosphides,[18,19] carbon materials,[20] ceramic materials[21]), and organic–inorganic composites (*e.g.*, metal–organic frameworks[22]), have been explored. Among these, poly[2,6-diimidazo(4,5-*b*:4′,5′-*e*)pyridinylene-1,4(2,5-dihydroxy)phenylene] (PIPD) represents a uniquely promising candidate due to its molecular structure. The rigid-rod polymer backbone with extended π-conjugation provides exceptional mechanical stability, while its *ortho*-positioned hydroxyl groups create polar domains that could facilitate lithium-ion coordination.[23,24] Simultaneously, the electron-deficient imidazole rings in PIPD's heterocyclic units offer potential Lewis acid sites for polysulfide interaction.[25] This combination of structural robustness, polar characteristics, and chemical affinity enables PIPD to function as a multifunctional separator material that simultaneously addresses both dendrite growth and polysulfide shuttle—a dual function rarely achieved by conventional coating materials.

Herein, we developed an ultrathin functional separator with abundant lithophilic sites, a uniformly distributed electric field, and strong interactions with LiPSs. Fabricated by blade-coating PP substrates with a 1 μm layer of PIPD nanofibers, the functional separator exhibits remarkable mechanical properties, achieving nearly double the tensile strength (91 MPa) of uncoated PP separators. The abundant nitrogen atoms and hydroxyl groups in the PIPD structure promote lithium-ion desolvation by the formation of instantaneous bonds to generate homogeneous lithium nucleation sites, thus enabling dendrite-free lithium deposition. The modification mechanism was elucidated using *in situ* optical microscopy and molecular dynamics simulations. Additionally, the positively charged imidazole groups in PIPD serve as Lewis acids, effectively immobilizing LiPSs and accelerating reaction kinetics. Consequently, Li||Cu cells assembled with PP@PIPD separators achieved a coulombic efficiency (CE) of 99.5% over 1000 cycles at 1 mA cm^{-2}. Moreover, Li–S batteries assembled with PP@PIPD delivered a specific capacity of 728.9 mAh g^{-1} over 450 cycles at 3C.

Results and discussion

PIPD nanofibers (PIPDNFs) were prepared from micro-sized PIPD fibers *via* a sol–gel conversion method.[26] Micrometer-sized PIPD fibers were dissolved in a homogeneous trifluoroacetic acid (TFA)/methanesulfonic acid (MSA) mixture, where the strong acids protonated nitrogen and oxygen atoms on the PIPD main chain, weakening intermolecular forces and enabling the fibers to exfoliate into nanofibers (Fig. 1a). This transformation reduced the fiber diameter from 800 μm to approximately 100 nm (Fig. 1b and Fig. S1, SI). The X-ray diffraction (XRD) profile reveals distinct Bragg diffraction peaks at 2θ = 10.5°, 20°, and 27.5°, corresponding to the (200), (110), and (110) planes of PIPDNFs, respectively (Fig. 1d).[27,28] The peaks were broader and less intense than those of PIPD microfibers (PIPDMFs), confirming the successful conversion to nanofibers.[28] The chemical structure of PIPD fibers was characterized by Fourier transform infrared (FTIR) spectroscopy, with absorption peaks at 2920 cm^{-1} attributed to secondary amino groups.[29] Notably, the nanofibers exhibited significant broadening of the hydroxyl stretching vibration peak within the 3200–3600 cm^{-1} region, indicating an increased number of free hydroxyl groups on the surface. This phenomenon originates from nanoscale effect-induced changes in the molecular chain orientation, resulting in an enhanced density of hydrogen-bonding networks among phenolic hydroxyl groups (Fig. 1e).[30,31] The increase in hydrogen bonding is attributed to the random nanofiber network structure. Table S1 (SI) presents a systematic analysis of characteristic peak assignments, while X-ray photoelectron spectroscopy (XPS) results confirm the elemental composition of PIPDNFs, with distinct peaks for O 1s, N 1s, and C 1s (Fig. S2, SI).[32] The C 1s spectra revealed peaks corresponding to C=N, C–C, C–N, and C–O, corroborating the structure of PIPDNFs (Fig. 1f).[29] The comprehensive experimental characterization results conclusively demonstrate the successful synthesis of PIPDNFs.

The PIPDNF slurry was uniformly coated with a specific thickness onto commercial PP (Celgard 2400) separators using a scalable blade-coating technique, followed by aging in an isopropyl alcohol (IPA) bath (Fig. 1c). During aging, IPA functioned as a Brønsted acid, promoting phase separation through proton removal from solvated PIPDNFs. Raman spectroscopy revealed that the characteristic peaks of the PP@PIPD separator retained the vibrational features characteristic of PIPDNFs, despite slight intensity reduction, confirming chemical structural preservation during coating (Fig. 1g). The key peaks at 1642, 1505, 1371, and 1313 cm^{-1} represent benzene ring vibrations, –C=N–, and C=C stretching.[33]

The tensile strength of the PP@PIPD separator, with a 1 μm PIPDNF coating (Fig. S3, SI), was significantly increased to 91 MPa, compared to the 44 MPa for the pristine PP separator.

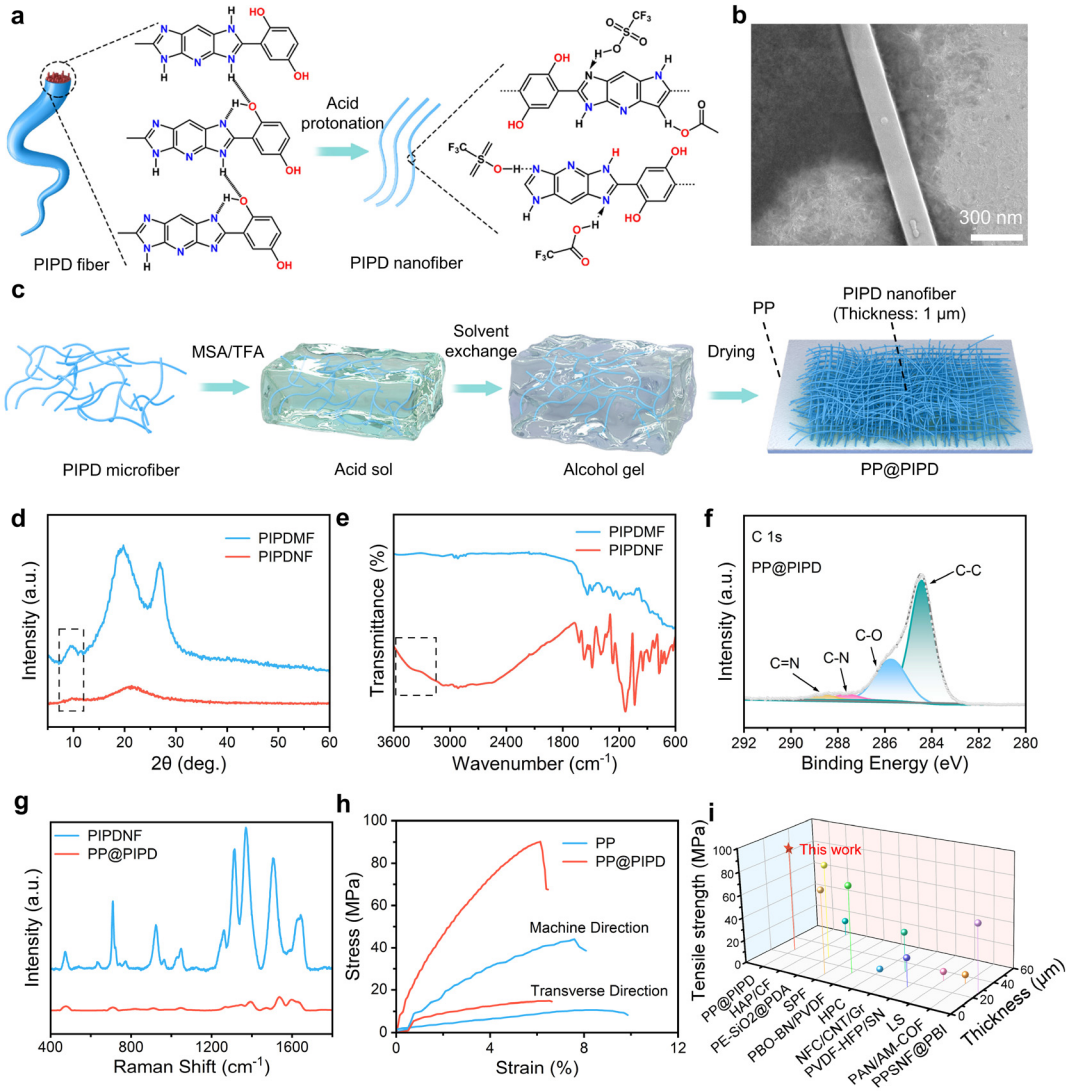

Fig. 1 Fabrication and characteristics of PP@PIPD separators. (a) Illustration of the preparation of PIPDNFs *via* MSA/TFA treatment. (b) The SEM image of PIPDNFs. (c) Schematic of the preparation process for PP@PIPD. (d) XRD of PIPDMFs and PIPDNFs. (e) FTIR spectra of PIPDMFs and PIPDNFs. (f) XPS spectra for C 1s of the PP@PIPD separator. (g) Raman spectra of PIPDNFs and PP@PIPD separators. (h) Stress–strain curves (transverse and machine directions) of the separators. (i) Comparison of machine tensile strength for PP@PIPD and other coated separators.

The performance enhancement originates from the three-dimensional hydrogen-bonding network formed by hydroxyl (–OH) and imino (–NH–) groups within the nanofiber architecture (Fig. 1h and Fig. S4, SI).[27] This tensile strength surpasses most previously reported values, highlighting the material's potential for large-scale applications (Fig. 1i).[34–43] Thermal stability is crucial for battery safety in commercial applications. While PP separators exhibited significant shrinkage at 155 °C, the PP@PIPD separator showed no deformation under similar conditions (Fig. S5, SI), due to the intrinsic synergistic interactions within the PIPD nanofiber coating. Despite its ultrathin nature, the PIPD coating mechanically reinforces the separator to redistribute thermal stress and restrict molecular mobility in the PP substrate. Additionally, the robust interfacial bonding at the PIPD and PP interface establishes a structurally integrated composite system, where the coating stabilizes the substrate by inhibiting polymer chain relaxation under heat. The high thermal resistance of PIPD further enhances this effect by acting as a thermal barrier, reducing heat transfer to the PP substrate and mitigating deformation. Together, these factors transform the separator into a composite structure with significantly improved thermal stability, effectively suppressing the shrinkage of the PP substrate. In addition, the poor compatibility of traditional polyolefin separators with polar electrolytes is a significant limitation in lithium-ion transport.[44,45] Contact angle (CA) measurements demonstrate improved wettability of the PP@PIPD separator (CA = 13°) compared to the pristine PP separator (CA = 52°), which originates from the increased surface exposure of –OH and –NH– functional groups on the PIPD polymer framework (Fig. S7, SI).[46]

To elucidate the regulatory mechanism of the separator-induced interfacial effect on the dynamic evolution of Li^+ solvation structures, classical molecular dynamics (MD) simulations were performed at the separator–electrolyte interface, with the representative configuration of simulation depicted in Fig. 2a and b. Radial distribution functions (RDFs) reveal that the peaks for Li^+–O ($TFSI^-$) are located at 1.91 Å and 1.93 Å for the PP and PP@PIPD separator systems, respectively, indicating a slight increase in the average distance for coordinated species in the PP@PIPD system (Fig. 2c and d). The stretching of Li^+–O ($TFSI^-$) bonds originates from PIPD's hydroxyl groups competitively coordinating with Li^+ (Li^+–O distance: 1.97 Å), which partially displaces $TFSI^-$ anions from the primary solvation shell. Notably, two peaks associated with Li^+–N (PIPD) and Li^+–O (PIPD) emerge at 1.93 Å and 1.97 Å, respectively, in the PP@PIPD system, demonstrating that PIPD affects the solvation structure of Li^+ despite its moderate Li^+ affinity. The imidazole nitrogen atoms further change the solvation environment through Lewis acid–base interactions, absorbing electron density from coordinated solvent molecules and reducing their binding strength with Li^+. This interaction between PIPD and Li^+ weakens the coordination between Li^+ and electrolyte components, resulting in a comparable bulk desolvation energy barrier of ~8.01 eV for both PP and PP@PIPD separators. However, at the interface, the PP separator shows a higher desolvation energy (6.88 eV) than the PP@PIPD separator (4.89 eV), indicating that the PP@PIPD separator facilitates Li^+ desolvation. This interfacial advantage stems from the synergistic effects of PIPD, where hydroxyl-induced solvation shell changes reduce Li^+ desolvation energy, while imidazole-induced charge redistribution weakens the interaction between lithium ions and solvents. The decrease in activation energy in Li||Li cells assembled with PP@PIPD separators compared to those assembled with PP provides additional experimental validation of this phenomenon (Fig. 2e and Fig. S8, SI).

Density functional theory (DFT) calculations were systematically conducted to investigate the chemical interaction mecha-

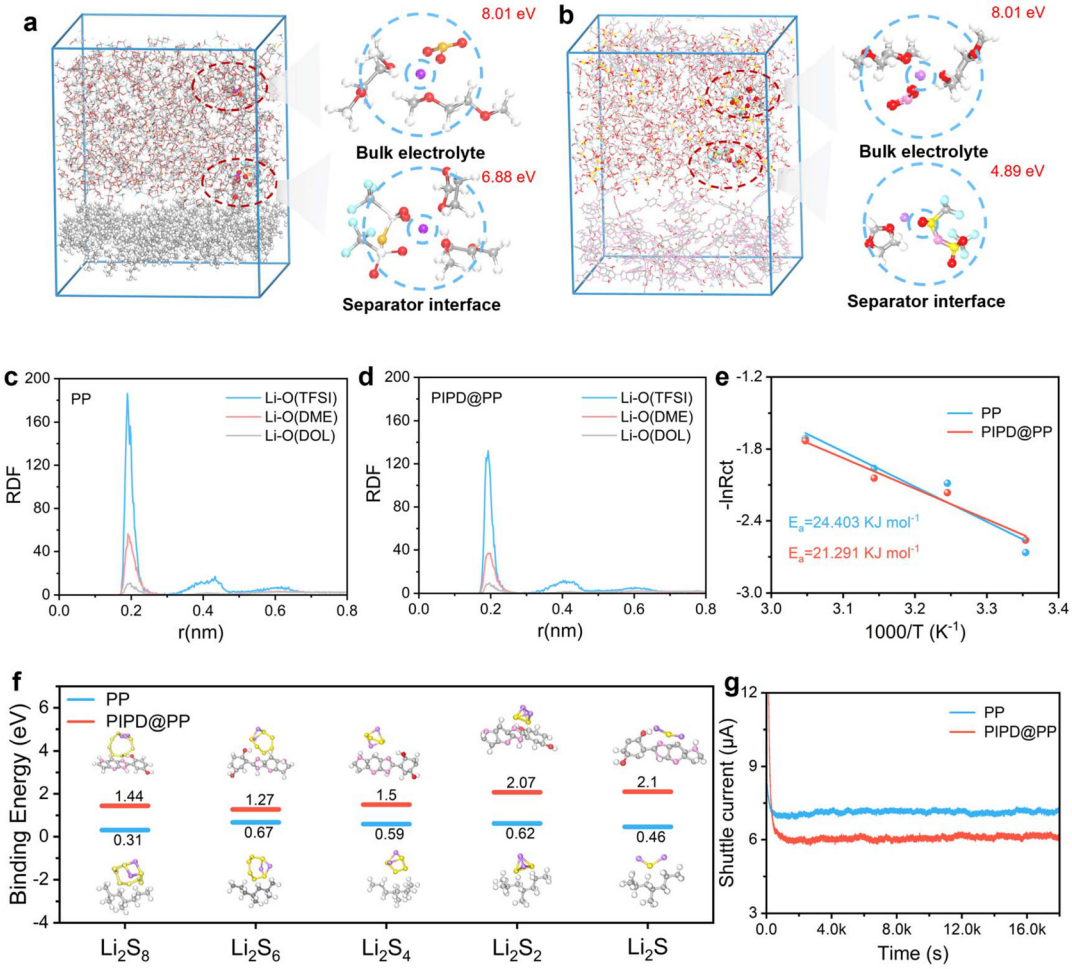

Fig. 2 Lithium-ion desolvation and interaction between PIPD and LiPSs. (a and b) MD simulation snapshots and lithium-ion desolvation energy for the bulk electrolyte and separator interfaces in PP and PP@PIPD separator systems, respectively. (c and d) Radial distribution function (RDF) of Li^+ in PP and PP@PIPD separator systems. (e) Activation energy for Li^+ transport in Li||Li cells. (f) Binding energy of PP and PP@PIPD separators with various Li_2S_x species (x = 1, 2, 4, 6, and 8). (g) Shuttle current.

nisms between PIPD and LiPSs (Fig. 2f). PIPD exhibits higher binding energies with Li_2S_8, Li_2S_6, Li_2S_4, Li_2S_2, and Li_2S (−1.44, −1.27, −1.5, −2.07, and −2.1 eV, respectively) compared to the bare PP (−0.31, −0.67, −0.59, −0.62, and −0.46 eV). These results confirm the superiority of PIPD to capture LiPSs, attributed to the electron-deficient imidazole groups, which exhibit strong adsorption capability. Consistent with these findings, H-type glass cell experiments show reduced polysulfide permeability in the presence of the PP@PIPD separator (Fig. S9, SI).

Quantitative evaluation of polysulfide shuttle suppression was conducted through shuttle current measurements, revealing that cells with conventional PP separators exhibited a 23.6% higher shuttle current (7.3 μA) compared to those with PP@PIPD (5.9 μA) (Fig. 2g). This effective shuttle suppression enhances cycling stability and electrochemical performance, demonstrating the unique superiority of the PP@PIPD separator.

A systematic investigation of lithium-ion transference number (t_{Li^+}) and ionic conductivity was performed to elucidate the influence of reduced desolvation energy on ion transport. The results demonstrate that the PP@PIPD separator enables significantly higher ionic conductivity, markedly exceeding that of the pristine PP separators (Fig. S10, SI). Similarly, the t_{Li^+} value of the PP@PIPD separator (0.72) was substantially higher than that of the PP separator (0.4) (Fig. 3a and Fig. S11, SI). Experimental results demonstrate that the PP@PIPD separator significantly enhances the diffusion kinetics of lithium-ion flux while optimizing its spatial distribution uniformity, thereby effectively improving the overall electrochemical performance.[47] Coulombic efficiency (CE) was measured to quantify Li plating/stripping behavior. The results demonstrate that the PP@PIPD separator maintains a stable CE of 99.5% over 1000 cycles (1 mA cm^{-2}/1 mAh cm^{-2}). In contrast, the cells with PP separators displayed a significant drop in CE after just 100 cycles (Fig. 3b). The nucleation overpotential (μ_n) in Li||Cu cells was systematically evaluated to elucidate the influence of the separators on Li deposition kinetics (Fig. 3c). The cells with the PP@PIPD separator exhibited a significantly lower μ_n value of 27 mV, which is 3.6 times smaller

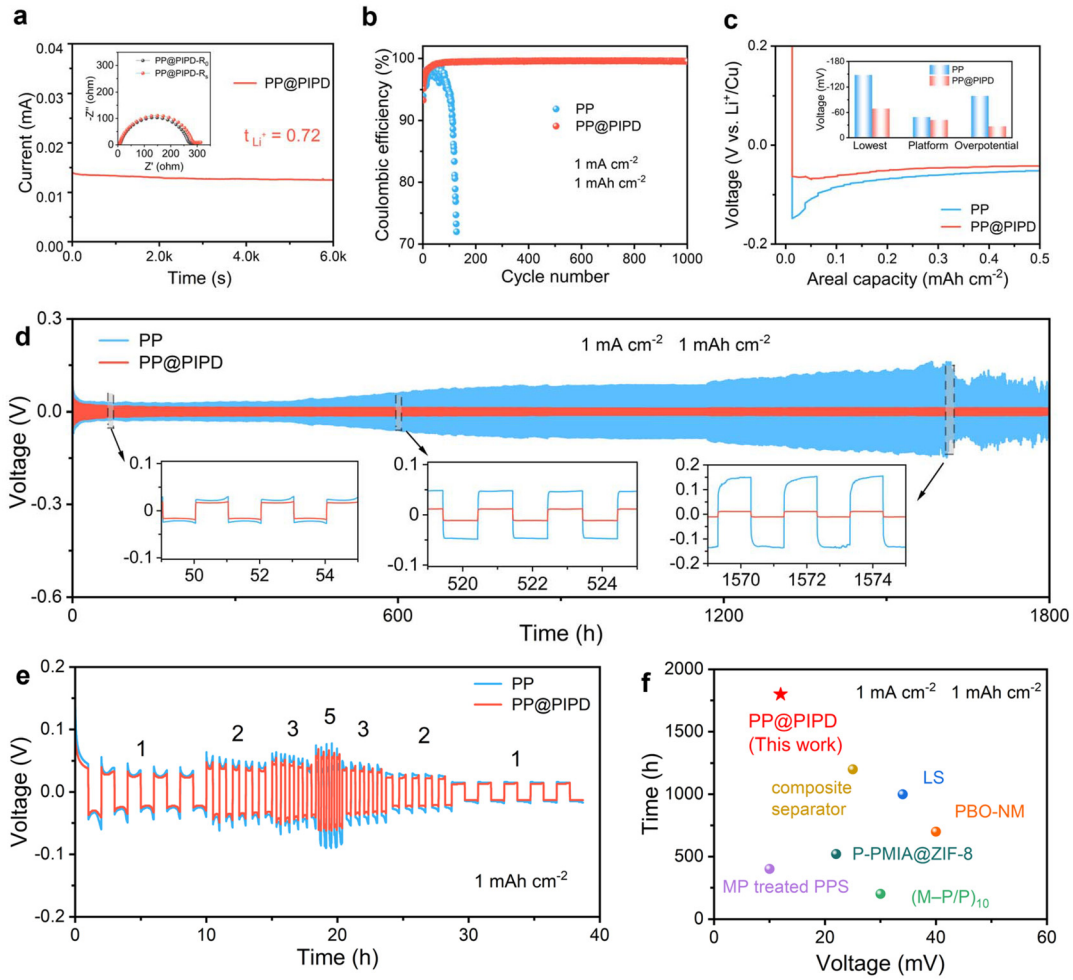

Fig. 3 Electrochemical performance of cells assembled with various separators. (a) Chronoamperometric response of Li||Li cells with PP@PIPD separators (inset: Nyquist plots). (b) CE profiles. (c) Nucleation overpotentials in Li||Li cells. (d) Voltage–time profiles and (e) rate performance of Li||Li cells. (f) Integrated performance comparison between this work and previously reported literature studies.

than the 99 mV observed for the cells with the PP separator. *In situ* optical microscopy was conducted to dynamically track real-time lithium dendrite growth in optically accessible Li symmetric cells under galvanostatic plating at 12.5 mA cm^{-2} (Fig. S12, SI). Prior to electrochemical cycling, distinct physical separation between the separator and the lithium anode was observed. After 10 minutes of plating, a porous and loosely packed lithium deposition layer formed on the Li surface when using the PP separator. In 30 minutes, the gap between the PP separator and the lithium foil was filled with severe lithium dendrites. In contrast, the PP@PIPD composite separator system exhibited a planar lithium deposition morphology with a uniform crystallographic orientation, while maintaining observable interfacial separation between the modified separator assembly and the metallic lithium anode throughout prolonged electrochemical cycling (Fig. S13, SI).

Li symmetric cells equipped with the PP@PIPD separator showed a stable polarization voltage (13 mV) (Fig. 3d). In contrast, the cells with PP separators demonstrated a markedly higher overpotential (1 mA cm^{-2}/1 mA cm^{-2}), thus deteriorating cycling performance. Remarkably, the cells with PP@PIPD separators maintained a lower polarization voltage at 1 mAh cm^{-2} across a broad current density range (1–5 mA cm^{-2}), implying superior electrochemical stability (Fig. 3e). Electrochemical impedance spectroscopy (EIS) measurements further confirm that Li||Li cells with PP@PIPD separators possess reduced interfacial resistance compared to those with the PP separator (Fig. S14, SI). These results highlight the superior cycling stability of lithium-ion/metal batteries with the PP@PIPD separator, surpassing most previously reported results in the literature (Fig. 3f).[26,34,48–51] The performance enhancement is based on the inherent capability of PIPD nanofibers to regulate Li^+ deposition behavior, forming a flat and compact Li plating layer. The effectiveness of the PP@PIPD separator was further confirmed by the deposition morphology of metallic lithium in Li symmetric cells after 25 cycles, assembled with various separators (Fig. S15, SI).

The Li plating/stripping process was investigated by cyclic voltammetry (CV) of Li||Cu cells (Fig. 4a). The cells with PP@PIPD separators exhibited a markedly enhanced current response compared to those with PP separators, indicating improved lithium-ion transport and deposition behavior. To further analyze the reaction kinetics, Tafel plots were recorded (Fig. 4b). Li||Li cells with PP@PIPD separators exhibited an

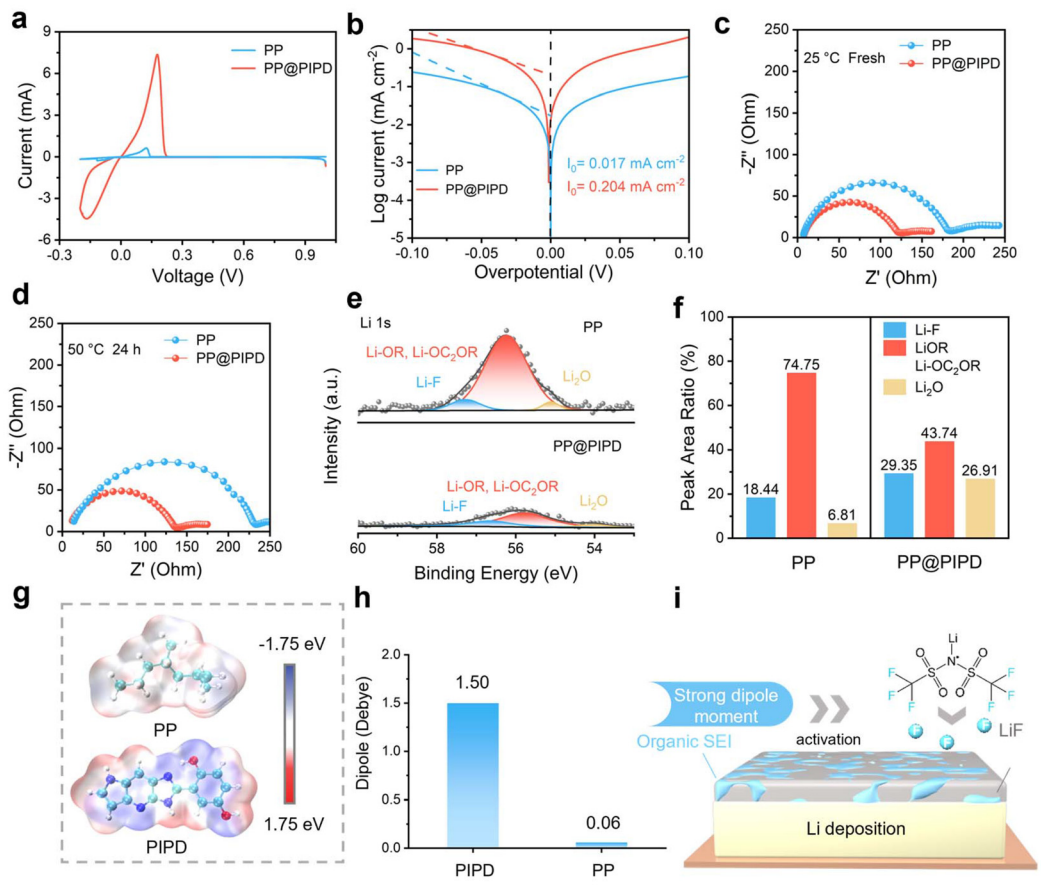

Fig. 4 The mechanism of SEI formation. (a) The CV profiles of Li||Cu cells. (b) Tafel polarization profiles. Nyquist profiles of Li symmetric cells at (c) 25 °C (fresh) and (d) after resting at 50 °C for 24 h. (e) XPS spectra for Li 1s of cycled lithium anodes. (f) Li content of SEI in Li symmetric cells. (g) Calculated ESP of PP and PIPD. (h) The dipole moment of PP and PIPD. (i) Schematic illustration of strong dipole moment's impact on the decomposition of LiTFSI for SEI formation.

exchange current density (i_0) of 0.145 mA cm^{-2}, significantly surpassing that of the cells with PP separators. This result is consistent with the observed enhancement in lithium-ion kinetics. EIS was conducted on Li||Li cells with various separators to assess interfacial resistance (R_{int}) before and after being rested at 50 °C for 24 hours. At room temperature, the cells with PP separators displayed a significantly higher R_{int} of 174.8 Ω compared to those utilizing the PP@PIPD separator (115.3 Ω) (Fig. 4c). After resting at 50 °C for 24 hours, the R_{int} of cells with the PP@PIPD separator showed only a slight increase (Fig. 4d), confirming its substantially improved interfacial stability. This improved stability originates from the strong interfacial interaction between the PIPD nanofiber coating and the lithium anode, which promotes uniform lithium deposition. XPS analysis of cycled Li anodes after three cycles revealed distinct SEI composition differences (Fig. 4e). The SEI formed with PP separators exhibited substantial organic components, primarily Li-OR and Li-OC$_2$OR,[52] indicative of electrolyte decomposition. In contrast, the Li anode with PP@PIPD separators exhibited a decreased proportion of organic components, indicating that the PP@PIPD separator promotes efficient Li^+ desolvation and minimizes solvent-induced corrosion of the Li anode. Furthermore, the SEI formed by the PP@PIPD separator showed elevated LiF content (Fig. 4f), which contributes to enhanced protection of the Li anode and stabilization of the SEI.

To elucidate the role of PIPD in LiTFSI decomposition and LiF formation, DFT simulations were performed, including electrostatic potential (ESP) mapping (Fig. 4g) and dipole moment calculations (Fig. 4h). The ESP maps revealed regions of electrophilicity (red) and nucleophilicity (blue), indicating that the strong dipole moments of the hydroxyl and nitrogen groups in PIPD promote electron transfer to the electrolyte. Compared to alkyl groups, the higher molecular polarity of PIPD facilitates the decomposition of LiTFSI, generating F^- species and forming substantial LiF in the SEI (Fig. 4i). In summary, the PP@PIPD separator improves lithium-ion kinetics and stabilizes the SEI by promoting LiTFSI decomposition and enhancing the formation of LiF, which protects the Li anode from degradation. These results demonstrate that PIPD is pivotal in enabling high-performance lithium metal batteries.

The LiPS shuttle effect and sluggish reduction kinetics represent the primary obstacles to enhancing Li–S battery performance. Wettability tests using Li_2S_6 electrolyte confirmed the strong adsorption interaction of PIPD with polysulfides. The Li_2S_6 electrolyte exhibited a contact angle (CA) of 21° on the PP@PIPD separator, which is a markedly lower value compared to the 34° observed on the pristine PP separator, indicating superior wettability and stronger adsorption by PIPD (Fig. 5a). Self-discharge testing was performed to elucidate the interfacial interactions between PIPD and LiPSs. After 20 cycles at 0.2C, the cells were charged to 2.8 V, rested for 72 h, and then cycled again for 20 cycles (Fig. S17, SI). During self-discharge, high-order polysulfides spontaneously convert to low-order polysulfides, causing a voltage drop.[53] Open-circuit voltage (OCV) monitoring during the relaxation period revealed that the cells with PP@PIPD composite separators showed an attenuated voltage decline compared to those with conventional PP separators, indicating reduced polysulfide migration and enhanced retention of active sulfur species (Fig. 5b). Furthermore, the charge–discharge profiles revealed that batteries with PP@PIPD separators showed reduced capacity loss compared to those with the conventional PP separators (Fig. S18, SI). Tafel corrosion tests were performed to assess the corrosion resistance of the separators. Li foil and stainless steel were employed as the anode and cathode, respectively, with different electrolyte components tested on either side of the cells. The cells with the PP@PIPD separator exhibited a more positive corrosion potential than those with the PP separator (Fig. 5c), suggesting that the parasitic reactions between the Li anode and the polysulfides were effectively suppressed. The PP@PIPD separator also facilitated faster Li^+ desolvation, promoting accelerated Li_2S deposition kinetics. To examine the liquid–solid conversion of LiPSs, chronoamperometric nucleation experiments were conducted using Li||Li_2S_8 cells, with carbon paper as the cathode and 0.2 M Li_2S_8 catholyte as the active material. The *i*–*t* curves reveal three stages: reduction of soluble Li_2S_8 and Li_2S_6 (orange and grey) and nucleation of Li_2S (blue or red). The PP@PIPD-based cells demonstrated a significantly higher Li_2S nucleation capacity (162.96 mAh g^{-1}) than the PP-based cells (54.56 mAh g^{-1}). Additionally, the morphology of Li_2S deposited on carbon paper showed a uniform nucleation size when using PP@PIPD separator, which favors the stable cycling performance of the full batteries (Fig. 5d and e). The electron-deficient imidazole groups in PIPD enhance polysulfide adsorption and facilitate rapid Li^+ desolvation. This dual effect not only enhances LiPS immobilization but also accelerates their nucleation kinetics at the cathode/LiPS interface, substantially boosting the discharge performance of Li–S batteries.

The galvanostatic intermittent titration technique (GITT) was employed to dynamically explore internal polarization during the discharge process. The PP@PIPD-assembled batteries exhibited a smaller working voltage drop, although both exhibited similar equilibrium voltages, indicating reduced polarization and faster cathode kinetics (Fig. 5f). XPS analysis demonstrated a higher sulfur content in the SEI of PP separator-based batteries (78%) compared to the PP@PIPD separator system (61%), indicating more severe parasitic interactions between LiPSs and the lithium metal anode in the PP separator system (Fig. 5g–i). Additionally, the proportion of F-containing species in the SEI formed with the PP@PIPD separator revealed that LiF was the dominant fluoride component (37%), further demonstrating the protective role of the PP@PIPD separator.

The imidazole functional groups in the PP@PIPD separator significantly enhance polysulfide adsorption, mitigating the shuttle effect and improving sulfur utilization efficiency. The PP@PIPD separator effectively suppresses parasitic reactions and promotes homogeneous Li_2S deposition, which results in an improvement in the cycling stability of Li–S batteries, as evi-

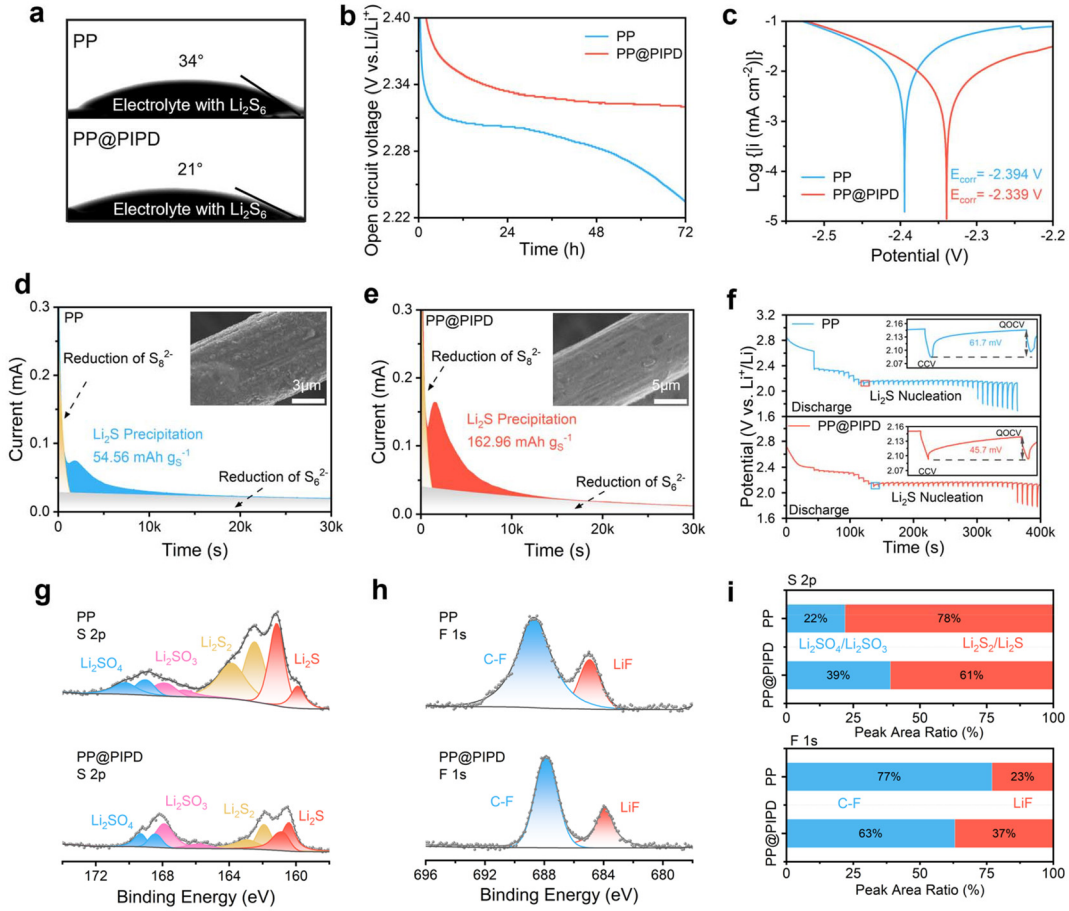

Fig. 5 Evaluation of shuttle inhibition and cathode kinetics of LiPSs with various separators. (a) The contact angle measurements of 10 mM Li_2S_6-containing electrolytes. (b) The OCV records of Li–S batteries. (c) Potentiodynamic polarization profiles of Li symmetric cells. Chronoamperometric discharge responses of full batteries assembled with (d) PP and (e) PP@PIPD separators at a constant voltage (2.03 V). Inset: The morphology of Li_2S deposited on carbon papers. (f) GITT curves. XPS of (g) S 2p and (h) F 1s of cycled Li anodes (5 cycles). (i) S (upper) and F (below) content of the SEI.

denced by their superior performance over extended cycles. The CV profiles of Li–S batteries assembled with PP and PP@PIPD separators (Fig. 6a) displayed three distinct peaks: Peak A: initial reduction of S_8 to long-chain Li_2S_x ($4 \leq x \leq 8$); Peak B: subsequent conversion to solid-phase Li_2S_2/Li_2S. Conversely, Peak C corresponds to the oxidative reconversion process, where Li_2S_2/Li_2S is electrochemically reverted to S_8.[54] The batteries assembled with PP@PIPD separators delivered higher peak intensities and reduced polarization in contrast to those with PP separators, suggesting that the deposition and reoxidation of Li_2S were significantly enhanced. Tafel analysis of Peak B showed a smaller slope for the PP@PIPD-based full cell (65.6 mV dec^{-1}) compared to the PP-based cell (165.6 mV dec^{-1}), further confirming enhanced Li_2S deposition kinetics (Fig. 6b).

EIS analysis was performed to analyze the reaction kinetics. The Nyquist plots of full batteries at 1C, both fresh and after 25 cycles, were characterized by a high-frequency semicircle related to charge transfer resistance (R_{ct}), and a linear Warburg impedance response in the low frequency region (Fig. 6c and Fig. S20, SI).[55] The batteries with PP@PIPD separators showed significantly lower R_{ct} after 25 cycles, demonstrating improved charge transfer and sulfur species utilization compared to batteries with PP separators. The rate performance of Li–S batteries equipped with PP@PIPD was compared with that of the batteries equipped with PP separators (Fig. 6d). The specific discharge capacities of the batteries with PP@PIPD separators at 0.2, 0.5, 1, 3, and 5C were 1169.1, 921.7, 843.5, 707.7, and 592.3 mAh g^{-1}, respectively. Conversely, the batteries equipped with PP separators displayed lower capacities of 1074.8, 819.6, 739.4, 609.3, and 444.8 mAh g^{-1} under the same conditions. The lower overpotentials and higher capacity retention at various rates further highlight the advantages of the PP@PIPD separator (Fig. 6e and Fig. S21, SI).

The discharge profiles exhibited two distinct voltage plateaus reflecting the sequential phase transitions from S_8 to Li_2S_4 (Q_1) and subsequently from Li_2S_4 to Li_2S (Q_2). The batteries with PP@PIPD separators achieved higher Q_1 and Q_2 values, with a Q_2/Q_1 ratio closer to the theoretical value (3), indicating more complete sulfur conversion and higher sulfur

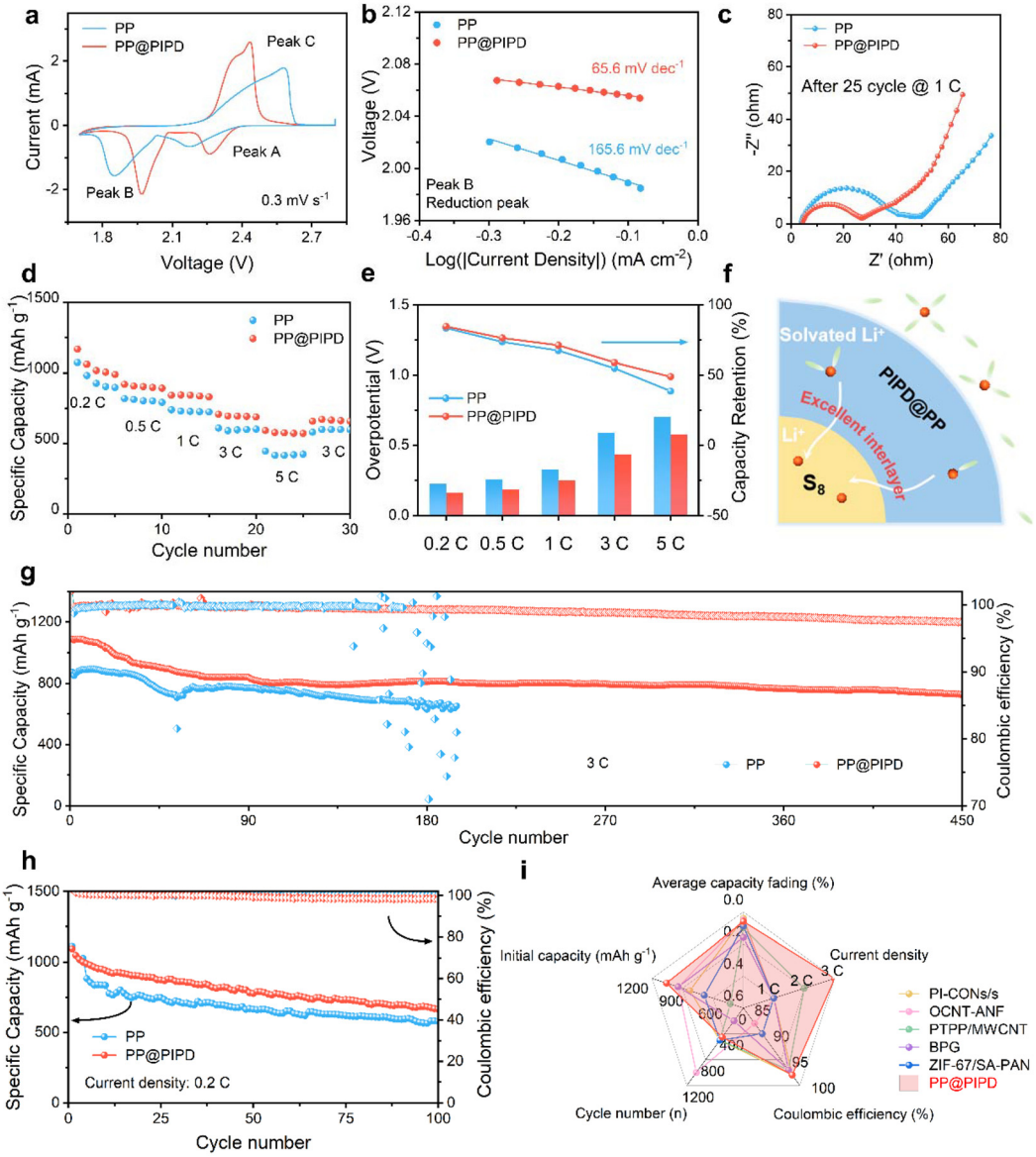

Fig. 6 Electrochemical characterization of Li–S batteries assembled with various separators. (a) CV profiles (0.3 mV s^{-1}). (b) Tafel polarization analysis of Peak B. (c) Nyquist curves for Li–S batteries after 25 charge–discharge cycles at 1C. (d) Rate performance. (e) The overpotential and capacity retention profiles at different current densities. (f) Working mechanism of multifunctional PP@PIPD separators. The cycling profiles of full batteries at (g) 3C and (h) 0.2C. (i) The comparison of integrated performance between this work and other reported fiber-based separators in Li–S batteries.

utilization (Fig. S22, SI). The cycling stability of Li–S batteries assembled with PP@PIPD separators was systematically assessed at 3C. The cells maintained exceptional capacity retention over 450 cycles with near-100% CE (Fig. 6g). At 0.2C, the cells with the PP@PIPD separator displayed an initial specific capacity of 1093.8 mAh g^{-1} (CE ≈ 100%), maintaining 665.5 mAh g^{-1} after 100 charge–discharge cycles. Comparatively, the cells assembled with the PP separator showed markedly inferior performance, sustaining 385.7 mAh g^{-1} with a significantly lower CE of 31.3% after the same number of cycles (Fig. 6h).

The surface morphology of lithium anodes was observed after cycling (Fig. S23, SI). After 500 cycles at 0.2C, lithium anodes paired with PP separators showed significant cracking, likely due to reactions between polysulfides and the Li anode. In contrast, anodes paired with PP@PIPD separators remained flat and smooth. Even after 1000 cycles, Li anodes with PP@PIPD separators maintained a smooth surface (Fig. S24, SI). PP@PIPD separators demonstrate comprehensive performance advantages over existing temperature-resistant fibrous separators in Li–S battery applications, including significantly improved capacity retention, enhanced initial discharge capacity, near-theoretical CE, and superior cycling stability (Fig. 6i).[56–60] The imidazole and hydroxyl groups in PIPD contribute to facilitating Li^+ desolvation, accelerating Li_2S precipitation, and stabilizing the sulfur utilization process.

Conclusion

In summary, the integration of a PIPD coating onto polypropylene separators presents an effective strategy to tackle critical challenges in Li–S batteries, including dendritic lithium growth and the polysulfide shuttle effect. The N atoms and hydroxyl groups in PIPD form instantaneous bonds that accelerate lithium-ion desolvation, enabling rapid and uniform lithium deposition. Additionally, the Lewis-acidic imidazole groups in PIPD exhibit strong interactions with LiPSs, effectively suppressing the shuttle effect and enhancing sulfur utilization. The PIPD-based separator demonstrated exceptional mechanical properties, achieving nearly double the tensile strength (91 MPa) of the uncoated PP separator with only a 1 μm PIPDNF coating. Electrochemical performance tests revealed remarkable stability and efficiency: the PP@PIPD separator demonstrates exceptional electrochemical performance, enabling Li||Li cells to maintain stable cycling for over 1800 hours at 1 mA cm^{-2}, Li||Cu cells to achieve a consistent 99.5% average coulombic efficiency throughout 1000 cycles. Notably, Li–S full batteries showed superior cycling durability with merely 32.6% capacity fade after 450 cycles at 3C. These results confirm the considerable potential of PIPD-modified separators in improving the performance, safety, and cycle life of Li–S batteries, paving the way for their practical application in next-generation energy storage systems.

Author contributions

Xu, G. contributed to the conceptual design, project management and resource support; Xu, G. and Cao, C. handled funding acquisition and provided guidance; Yang, H. carried out material preparation and electrochemical testing; Liu, H. performed material synthesis and analytical characterization; Zhang, J. performed theoretical computational simulations; Yang, H., Liu, H. and Zhang, J. drafted the manuscript; Zhu, M., Zhu, L., Zhang, T., Zhu, X. and Liu, Z. participated in the guidance and revision of the paper.

Conflicts of interest

The authors declare no competing financial interests or personal relationships to disclose.

Data availability

The data that support the findings of this article are available from the corresponding author upon reasonable request.

All data needed to evaluate the conclusions in this paper are present in the main manuscript or its SI. The DRT analysis software used in this study was developed by the research group of Francesco Ciucci, and is available for download at [https://github.com/ciuccislab]. Supplementary information (SI) is available. See DOI: **https://doi.org/10.1039/d5eb00085h**

Acknowledgements

This work was supported by the National Key Research and Development Program of China (2022YFB3803502), the National Natural Science Foundation of China (52103076 and 52203005), the Fundamental Research Funds for the Central Universities (2232025A-05), the Interdisciplinary Frontier Innovation Team Development Special Fund of Donghua University, the Shanghai Rising-Star Program (24QA2700100), the International Cooperation Fund of the Science and Technology Commission of Shanghai Municipality (24520713300), and the Joint Funds of the National Natural Science Foundation of China (U23B2079). C. C. acknowledges the support from USDA-NIFA (2021-67021-42113) and Case Western Reserve University.

References

1 L. Cheng, J. Liu, H. Wang, Y. Guo, A. Shao, Y. Li, Z. Wang, Y. Zhang, J. Tang, C. Li and Y. Ma, A Lightweight, Li Supplementary and Lithiophilic Interface Enables Anode-Less Lithium Metal Battery Prototyping, *EES Batter.*, 2025, **1**(3), 555–565, DOI: **10.1039/D5EB00042D**.

2 D. Larcher and J. M. Tarascon, Towards Greener and More Sustainable Batteries for Electrical Energy Storage, *Nat. Chem.*, 2015, **7**(1), 19–29, DOI: **10.1038/nchem.2085**.

3 J. T. Frith, M. J. Lacey and U. Ulissi, A Non-Academic Perspective on the Future of Lithium-Based Batteries, *Nat. Commun.*, 2023, **14**(1), 420, DOI: **10.1038/s41467-023-35933-2**.

4 Z. Shi, Z. Tian, D. Guo, Y. Wang, Z. Bayhan, A. S. Alzahrani and H. N. Alshareef, Kinetically Favorable Li–S Battery Electrolytes, *ACS Energy Lett.*, 2023, **8**(7), 3054–3080, DOI: **10.1021/acsenergylett.3c00826**.

5 L. Wang, K. Yue, Q. Qiao, Z. Zhao, Y. Xu, L. Pan, Y. Liu, H. Li and B. Zhu, In Situ Self-Polymerization of Thioctic Acid Enabled Interphase Engineering Towards High-Performance Lithium–Sulfur Battery, *Adv. Energy Mater.*, 2025, **15**(1), 2402617, DOI: **10.1002/aenm.202402617**.

6 H. Yuan, J. Zheng, G. Lu, L. Zhang, T. Yan, J. Luo, Y. Wang, Y. Liu, T. Guo, Z. Wang, J. Nai and X. Tao, Formation of 2D Amorphous Lithium Sulfide Enabled by Mo_2C Clusters Loaded Carbon Scaffold for High-Performance Lithium Sulfur Batteries, *Adv. Mater.*, 2024, **36**(28), 2400639, DOI: **10.1002/adma.202400639**.

7 H. Chen, G. Zhou, D. Boyle, J. Wan, H. Wang, D. Lin, D. Mackanic, Z. Zhang, S. C. Kim, H. R. Lee, H. Wang, W. Huang, Y. Ye and Y. Cui, Electrode Design with Integration of High Tortuosity and Sulfur-Philicity for High-Performance Lithium-Sulfur Battery, *Matter*, 2020, **2**(6), 1605–1620, DOI: **10.1016/j.matt.2020.04.011**.

8 M. Xu, Q. Zhu, Y. Li, Y. Gao, N. Sun and B. Xu, Atom-Dominated Relay Catalysis of High-Entropy MXene Promotes Cascade Polysulfide Conversion for Lithium–

Sulfur Batteries, *Energy Environ. Sci.*, 2024, **17**(20), 7735–7748, DOI: 10.1039/d4ee03402c.

9 Y. Liu, L. Xu, Y. Yu, M. He, H. Zhang, Y. Tang, F. Xiong, S. Gao, A. Li, J. Wang, S. Xu, D. Aurbach, R. Zou and Q. Pang, Stabilized Li-S Batteries with Anti-Solvent-Tamed Quasi-Solid-State Reaction, *Joule*, 2023, **7**(9), 2074–2091, DOI: 10.1016/j.joule.2023.07.013.

10 M. Chen, M. Shao, J. Jin, L. Cui, H. Tu and X. Fu, Configurational and Structural Design of Separators toward Shuttling-Free and Dendrite-Free Lithium-Sulfur Batteries: A Review, *Energy Storage Mater.*, 2022, **47**, 629–648, DOI: 10.1016/j.ensm.2022.02.051.

11 Z. Ju, J. Nai, Y. Wang, T. Liu, J. Zheng, H. Yuan, O. Sheng, C. Jin, W. Zhang, Z. Jin, H. Tian, Y. Liu and X. Tao, Biomacromolecules Enabled Dendrite-Free Lithium Metal Battery and Its Origin Revealed by Cryo-Electron Microscopy, *Nat. Commun.*, 2020, **11**(1), 488, DOI: 10.1038/s41467-020-14358-1.

12 Z. Li, P. Qian, H. Li, H. Xiao, J. Chen and G. Li, Phosphorylated Cellulose Nanofibers Establishing Reliable Ion-Sieving Barriers for Durable Lithium-Sulfur Batteries, *J. Energy Chem.*, 2024, **92**, 619–628, DOI: 10.1016/j.jechem.2024.02.002.

13 C. Wang, W. Li, Y. Jin, J. Liu, H. Wang and Q. Zhang, Functional Separator Enabled by Covalent Organic Frameworks for High-Performance Li Metal Batteries, *Small*, 2023, **19**(28), 2300023, DOI: 10.1002/smll.202300023.

14 Y. Deng, A. Hussain, W. Raza, L. Ao, K. Zong, J. Zhao, W. Liu, P. Ye, A. Ramiere, X. Cai, D. Liu and J. Shen, Morphological Modulation of the PBI Membrane and Performance Optimization for Li-Metal Battery, *Chem. Eng. J.*, 2023, **474**, 145800, DOI: 10.1016/j.cej.2023.145800.

15 Y. Deng, A. Hussain, W. Raza, X. Cai, D. Liu and J. Shen, Review on Current Development of Polybenzimidazole Membrane for Lithium Battery, *J. Energy Chem.*, 2024, **91**, 579–608, DOI: 10.1016/j.jechem.2023.12.044.

16 D. Guo, L. Mu, F. Lin and G. Liu, Mesoporous Polyimide Thin Films as Dendrite-Suppressing Separators for Lithium–Metal Batteries, *ACS Nano*, 2024, **18**(1), 155–163, DOI: 10.1021/acsnano.3c04159.

17 J. P. Lowen, T. Insinna, T. V. Beatriceveena, M. P. Stockham, B. Dong, S. J. Day, C. P. Grey, E. Kendrick, P. R. Slater, P. A. Anderson and J. W. Makepeace, Probing the Electrochemical Behaviour of Lithium Imide as an Electrolyte for Solid-State Batteries, *EES Batter.*, 2025, **1**(3), 527–540, DOI: 10.1039/D5EB00058K.

18 J. Li, G. Li, R. Wang, Q. He, W. Liu, C. Hu, H. Zhang, J. Hui and F. Huo, Boron-Doped Dinickel Phosphide to Enhance Polysulfide Conversion and Suppress Shuttling in Lithium–Sulfur Batteries, *ACS Nano*, 2024, **18**(27), 17774–17785, DOI: 10.1021/acsnano.4c03315.

19 C. Zhou, M. Hong, N. Hu, J. Yang, W. Zhu, L. Kong and M. Li, Bi-Metallic Coupling-Induced Electronic-State Modulation of Metal Phosphides for Kinetics-Enhanced and Dendrite-Free Li–S Batteries, *Adv. Funct. Mater.*, 2023, **33**(14), 2213310, DOI: 10.1002/adfm.202213310.

20 B. Yuan, Y. Feng, X. Qiu, Y. He, L. Dong, S. Zhong, J. Liu, Y. Liang, Y. Liu, H. Xie, Z. Liu, J. Han and W. He, A Safe Separator with Heat-Dispersing Channels for High-Rate Lithium-Ion Batteries, *Adv. Funct. Mater.*, 2024, **34**(9), 2308929, DOI: 10.1002/adfm.202308929.

21 J. Wang, K. Jia, J. Ma, Z. Liang, Z. Zhuang, Y. Zhao, B. Li, G. Zhou and H. M. Cheng, Sustainable Upcycling of Spent $LiCoO_2$ to an Ultra-Stable Battery Cathode at High Voltage, *Nat. Sustain.*, 2023, **6**(7), 797–805, DOI: 10.1038/s41893-023-01094-9.

22 Y. He, Y. Qiao, Z. Chang and H. Zhou, The Potential of Electrolyte Filled MOF Membranes as Ionic Sieves in Rechargeable Batteries, *Energy Environ. Sci.*, 2019, **12**(8), 2327–2344, DOI: 10.1039/C8EE03651A.

23 Y. Takahashi, Neutron Structure Analysis of Poly(pyridobisimidazole) (PIPD), *Macromolecules*, 2002, **35**(10), 3942–3945, DOI: 10.1021/ma0121520.

24 J. C. L. Hageman, G. A. de Wijs, R. A. de Groot and E. A. Klop, The Role of the Hydrogen Bonding Network for the Shear Modulus of PIPD, *Polymer*, 2005, **46**(21), 9144–9154, DOI: 10.1016/j.polymer.2005.07.027.

25 A. Pogoreltsev, Y. Tulchinsky, N. Fridman and M. Gandelman, Nitrogen Lewis Acids, *J. Am. Chem. Soc.*, 2017, **139**(11), 4062–4067, DOI: 10.1021/jacs.6b12360.

26 X. Hao, J. Zhu, X. Jiang, H. Wu, J. Qiao, W. Sun, Z. Wang and K. Sun, Ultrastrong Polyoxyzole Nanofiber Membranes for Dendrite-Proof and Heat-Resistant Battery Separators, *Nano Lett.*, 2016, **16**(5), 2981–2987, DOI: 10.1021/acs.nanolett.5b05133.

27 Y. Takahashi, Crystal Structure of Poly(pyridobisimidazole), PIPD, *Macromolecules*, 2003, **36**(23), 8652–8655, DOI: 10.1021/ma030289f.

28 E. A. Klop and M. Lammers, XRD Study of the New Rigid-Rod Polymer Fibre PIPD, *Polymer*, 1998, **39**(24), 5987–5998, DOI: 10.1016/s0032-3861(97)10187-2.

29 N. Taloub, L. Liu, J. Li, N. Rahoui, Y. Huang and M. Hegazy, 3D Coating Layers of Polyhydroquinone Diimidazopyridine (PIPD) Fibers to Improve Their Mechanical, Interfacial and Antimicrobial Properties, *Mater. Chem. Phys.*, 2021, **273**, 125124, DOI: 10.1016/j.matchemphys.2021.125124.

30 B. Athokpam, S. G. Ramesh and R. H. McKenzie, Effect of Hydrogen Bonding on the Infrared Absorption Intensity of OH Stretch Vibrations, *Chem. Phys.*, 2017, **488–489**, 43–54, DOI: 10.1016/j.chemphys.2017.03.006.

31 P. K. Deshmukh, K. P. Ramani, S. S. Singh, A. R. Tekade, V. K. Chatap, G. B. Patil and S. B. Bari, Stimuli-Sensitive Layer-by-Layer (LbL) Self-Assembly Systems: Targeting and Biosensory Applications, *J. Controlled Release*, 2013, **166**(3), 294–306, DOI: 10.1016/j.jconrel.2012.12.033.

32 N. Taloub, L. Liu, N. Rahoui, M. Hegazy and Y. Huang, Grafting Multi-Walled Carbon Nanotubes (MWCNTs) into PIPD Fiber for Enhancing Mechanical and Interfacial Performance, *Polym. Test.*, 2019, **75**, 344–349, DOI: 10.1016/j.polymertesting.2019.02.016.

33 J. Sirichaisit and R. J. Young, Tensile and Compressive Deformation of Polypyridobisimidazole (PIPD)-Based 'M5'

Rigid-Rod Polymer Fibres, *Polymer*, 1999, **40**(12), 3421–3431, DOI: 10.1016/s0032-3861(98)00561-8.

34 K. Wang, J. Duan, X. Chen, J. Wang, J. Li, L. Jiang, W. Yan, W. Lyu and Y. Liao, Nanofibrous Covalent Organic Frameworks Based Hierarchical Porous Separators for Fast-Charging and Thermally Stable Lithium Metal Batteries, *Adv. Energy Mater.*, 2024, **14**(25), 2401146, DOI: 10.1002/aenm.202401146.

35 T. Wang, Q. Liu, J. Zhou, X. Wang and B. Lu, Natural Supra-Molecular Structure Engineering for High-Performance Potassium Batteries Separator, *Adv. Energy Mater.*, 2022, **12**(44), 2202357, DOI: 10.1002/aenm.202202357.

36 H. Li, D. Wu, J. Wu, L. Y. Dong, Y. J. Zhu and X. Hu, Flexible, High-Wettability and Fire-Resistant Separators Based on Hydroxyapatite Nanowires for Advanced Lithium-Ion Batteries, *Adv. Mater.*, 2017, **29**(44), 1703548, DOI: 10.1002/adma.201703548.

37 X. Li, J. Zhang, X. Guo, C. Peng, K. Song, Z. Zhang, L. Ding, C. Liu, W. Chen and S. Dou, An Ultrathin Nonporous Polymer Separator Regulates Na Transfer toward Dendrite-Free Sodium Storage Batteries, *Adv. Mater.*, 2023, **35**(15), 2203547, DOI: 10.1002/adma.202203547.

38 L. Zuo, Q. Ma, P. Xiao, Q. Guo, W. Xie, D. Lu, X. Yun, C. Zheng and Y. Chen, Upgrading the Separators Integrated with Desolvation and Selective Deposition toward the Stable Lithium Metal Batteries, *Adv. Mater.*, 2024, **36**(13), 2311529, DOI: 10.1002/adma.202311529.

39 J. Dai, C. Shi, C. Li, X. Shen, L. Peng, D. Wu, D. Sun, P. Zhang and J. Zhao, A Rational Design of Separator with Substantially Enhanced Thermal Features for Lithium-Ion Batteries by the Polydopamine–Ceramic Composite Modification of Polyolefin Membranes, *Energy Environ. Sci.*, 2016, **9**(10), 3252–3261, DOI: 10.1039/C6EE01219A.

40 Y. Ji, L. Dong, J. Liu, H. Xie, S. Zhong, C. Yang, J. Han and W. He, A Li^+-Flux-Homogenizing Separator for Long-term Cycling of Li Metal Anodes, *Energy Environ. Sci.*, 2024, **17**(12), 4078–4089, DOI: 10.1039/D4EE00115J.

41 H. Lu, A. Du, X. Lin, Z. Zhang, S. Liu, Y. Xie, W. Li, J. Song, Y. Lu, W. Chen, C. Yang and Q. H. Yang, Rationally Coupling Thermal Tolerance, Thermal Conductance, and Overheating-Response in a Separator for Safe Batteries, *Energy Environ. Sci.*, 2024, **17**(20), 7860–7869, DOI: 10.1039/D4EE02302A.

42 J. Qian, Q. Chen, M. Hong, W. Xie, S. Jing, Y. Bao, G. Chen, Z. Pang, L. Hu and T. Li, Toward Stretchable Batteries: 3D-printed Deformable Electrodes and Separator Enabled by Nanocellulose, *Mater. Today*, 2022, **54**, 18–26, DOI: 10.1016/j.mattod.2022.02.015.

43 Z. Zou, M. Yin, P. Yin, Z. Hu, D. Wang and H. Pu, Facile Preparation of Surface-Modified Polypropylene Nanofiber Separators with Enhanced Ionic Transport and Welding Performance for Lithium-Ion Batteries, *Nano Energy*, 2024, **127**, 109774, DOI: 10.1016/j.nanoen.2024.109774.

44 Y. H. Liu, L. X. Li, A. Y. Wen, F. F. Cao and H. Ye, A Janus MXene/MOF Separator for the All-In-One Enhancement of Lithium-Sulfur Batteries, *Energy Storage Mater.*, 2023, **55**, 652–659, DOI: 10.1016/j.ensm.2022.12.028.

45 C. Yuan, X. Yang, P. Zeng, J. Mao, K. Dai, L. Zhang and X. Sun, Recent Progress of Functional Separators with Catalytic Effects for High-Performance Lithium-Sulfur Batteries, *Nano Energy*, 2021, **84**, 105928, DOI: 10.1016/j.nanoen.2021.105928.

46 Q. Jin, K. Zhao, L. Wu, L. Li, L. Kong and X. Zhang, Enhancing Li Cycling Coulombic Efficiency while Mitigating "Shuttle Effect" of Li-S Battery through Sustained Release of $LiNO_3$, *J. Energy Chem.*, 2023, **84**, 22–29, DOI: 10.1016/j.jechem.2023.05.020.

47 Y. Wen, J. Ding, J. Liu, M. Zhu and R. Hu, A Separator Rich in SnF_2 and NO_3^- Directs an Ultra-Stable Interface toward High Performance Li Metal Batteries, *Energy Environ. Sci.*, 2023, **16**(7), 2957–2967, DOI: 10.1039/d3ee00664f.

48 D. Han, X. Wang, Y. N. Zhou, J. Zhang, Z. Liu, Z. Xiao, J. Zhou, Z. Wang, J. Zheng, Z. Jia, B. Tian, J. Xie, Z. Liu and W. Tang, A Graphene-Coated Thermal Conductive Separator to Eliminate the Dendrite-Induced Local Hotspots for Stable Lithium Cycling, *Adv. Energy Mater.*, 2022, **12**(25), 2201190, DOI: 10.1002/aenm.202201190.

49 J. Wu, H. Zeng, X. Li, X. Xiang, Y. Liao, Z. Xue, Y. Ye and X. Xie, Ultralight Layer-by-Layer Self-Assembled MoS_2-Polymer Modified Separator for Simultaneously Trapping Polysulfides and Suppressing Lithium Dendrites, *Adv. Energy Mater.*, 2018, **8**(35), 1802430, DOI: 10.1002/aenm.201802430.

50 J. Liu, J. Wang, L. Zhu, X. Chen, G. Yi, Q. Ma, S. Sun, N. Wang, X. Cui, Q. Chai, J. Feng and W. Yan, In Situ Grown MOFs and PVDF-HFP Co-Modified Aramid Gel Nanofiber Separator for High-Safety Lithium–Sulfur Batteries, *J. Mater. Chem. A*, 2022, **10**(26), 14098–14110, DOI: 10.1039/D2TA03301A.

51 M. Kim, S. Y. Hong, J. Bang and S. S. Lee, Highly Sustainable Polyphenylene Sulfide Membrane of Tailored Porous Architecture for High-performance Lithium-Ion Battery Applications, *Mater. Today Adv.*, 2021, **12**, 100186, DOI: 10.1016/j.mtadv.2021.100186.

52 J. Tan, J. Matz, P. Dong, J. Shen and M. Ye, A Growing Appreciation for the Role of LiF in the Solid Electrolyte Interphase, *Adv. Energy Mater.*, 2021, **11**(16), 2100046, DOI: 10.1002/aenm.202100046.

53 X. Dai, G. Lv, Z. Wu, X. Wang, Y. Liu, J. Sun, Q. Wang, X. Xiong, Y. Liu, C. Zhang, S. Xin, Y. Chen and T. Zhou, Flexible Hierarchical Co-Doped NiS_2@CNF-CNT Electron Deficient Interlayer with Grass-Roots Structure for Li–S Batteries, *Adv. Energy Mater.*, 2023, **13**(21), 2300452, DOI: 10.1002/aenm.202300452.

54 Z. Qiao, Y. Zhang, Z. Meng, Q. Xie, L. Lin, H. Zheng, B. Sa, J. Lin, L. Wang and D. L. Peng, Anchoring Polysulfides and Accelerating Redox Reaction Enabled by Fe-Based Compounds in Lithium–Sulfur Batteries, *Adv. Funct. Mater.*, 2021, **31**(21), 2100970, DOI: 10.1002/adfm.202100970.

55 C. Fan, R. Yang, Y. Huang, L. Mao, Y. Yang, L. Gong, X. Dong, Y. Yan, Y. Zou, L. Zhong and Y. Xu, Graphene Quantum Dots as Sulfiphilic and Lithiophilic Mediator

toward High Stability and Durable Life Lithium-Sulfur Batteries, *J. Energy Chem.*, 2023, **85**, 254–266, DOI: **10.1016/j.jechem.2023.06.030**.

56 Z. Li, Y. Sun, X. Wu, H. Yuan, Y. Yu and Y. Tan, Boosting Adsorption and Catalysis of Polysulfides by Multifunctional Separator for Lithium–Sulfur Batteries, *ACS Energy Lett.*, 2022, **7**(12), 4190–4197, DOI: **10.1021/acsenergylett.2c02232**.

57 S. Hu, M. Yi, X. Huang, D. Wu, B. Lu, T. Wang, N. Li, Z. Zhu, X. Liu and J. Zhang, Cobalt-Doped Porphyrin-Based Porous Organic Polymer-Modified Separator for High-Performance Lithium–Sulfur Batteries, *J. Mater. Chem. A*, 2021, **9**(5), 2792–2805, DOI: **10.1039/D0TA10607K**.

58 H. Duan, K. Li, M. Xie, J. M. Chen, H. G. Zhou, X. Wu, G. H. Ning, A. I. Cooper and D. Li, Scalable Synthesis of Ultrathin Polyimide Covalent Organic Framework Nanosheets for High-Performance Lithium–Sulfur Batteries, *J. Am. Chem. Soc.*, 2021, **143**(46), 19446–19453, DOI: **10.1021/jacs.1c08675**.

59 H. Pei, X. Guan, X. Chen, Y. Chen, Y. Yang, Y. Wen, H. Nie, L. Chang, X. Zhou, X. Xie, L. Ye and Y. W. Mai, Multifunctional Tri-Layer Aramid Nanofiber Composite Separators for High-Energy-Density Lithium-Sulfur Batteries, *Nano Energy*, 2024, **126**, 109680, DOI: **10.1016/j.nanoen.2024.109680**.

60 C. Sun, J. Sheng, Q. Zhang, R. Gao, Z. Han, C. Li, X. Xiao, L. Qiu and G. Zhou, Self-Extinguishing Janus Separator with High Safety for Flexible Lithium-Sulfur Batteries, *Sci. China Mater.*, 2022, **65**(8), 2169–2178, DOI: **10.1007/s40843-022-2034-5**.